Article

Current Biology

Evidence for Myelin Sheath Remodeling in the CNS Revealed by *In Vivo* Imaging

Graphical Abstract

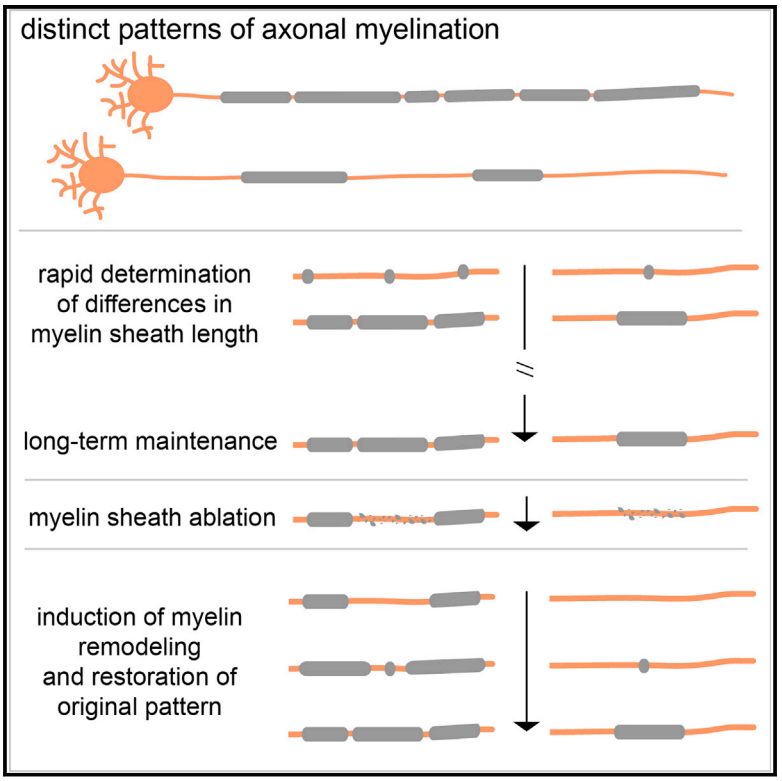

Highlights

- Differences in myelin sheath length are established in a few days after initiation
- Mature myelin sheaths continue extending to compensate for overall body growth
- Axon myelination patterns remain stable for long periods of time
- Myelin sheath ablation induces remodeling to restore the original myelin pattern

Authors

Franziska Auer, Stavros Vagionitis, Tim Czopka

Correspondence

tim.czopka@tum.de

In Brief

Auer et al. use zebrafish live imaging to investigate how axon myelination patterns with sheaths of different length are formed over time. Their work reveals that upon ablation of neighboring sheaths, myelin can plastically remodel to restore the original pattern, indicating a homeostatic regulation of myelin sheath positioning along axons.

Auer et al., 2018, Current Biology *28*, 549–559
February 19, 2018
https://doi.org/10.1016/j.cub.2018.01.017

CellPress

Current Biology
Article

CellPress

Evidence for Myelin Sheath Remodeling in the CNS Revealed by *In Vivo* Imaging

Franziska Auer,[1,3] Stavros Vagionitis,[1] and Tim Czopka[1,2,3,4,*]
[1]Institute of Neuronal Cell Biology, Technical University of Munich, Biedersteiner Strasse 29, 80802 Munich, Germany
[2]Munich Cluster of Systems Neurology (SyNergy), Feodor-Lynen Strasse 17, 81377 Munich, Germany
[3]Graduate School of Systemic Neurosciences (GSN), Ludwig-Maximilian University of Munich, Großhaderner Strasse 2, 82152 Planegg-Martinsried, Germany
[4]Lead Contact
*Correspondence: tim.czopka@tum.de
https://doi.org/10.1016/j.cub.2018.01.017

SUMMARY

The length of myelin sheaths affects conduction speed along axons and information propagation. It has recently become clear that myelin may be adaptively modified to modulate circuit function, implying that length remodeling of myelin sheaths should occur. However, direct evidence for such events is lacking. We have investigated how myelination patterns are formed, maintained, and remodeled using long-term imaging and myelin ablation in zebrafish. We demonstrate that length differences between myelin sheaths are established by rapid and variable growth within 3 days after their formation, independently of their time of formation, and even along discontinuously myelinated axons. Afterward, sheaths continue extending at similar rates to compensate for overall animal growth. In consequence, once axon myelination patterns are established, they are maintained over long periods of time. We tested whether mature myelin sheaths can remodel by removing individual sheaths from single axons by targeted ablation. Remarkably, extensive changes in sheath length and number occurred, which frequently restored the original myelination pattern. Our results show that axons can control myelin growth and remodeling, and we provide evidence for a homeostatic control of axon myelination patterns by maintenance and remodeling of myelin sheath length, with implications for circuit development, function, and repair.

INTRODUCTION

In the CNS of vertebrates, rapid and energy-efficient nerve conduction along axons is achieved through their myelination by oligodendrocytes [1]. The exact speed of axonal conduction depends on several molecular and structural parameters, including the thickness of axon and surrounding myelin, as well as the distance between nodes of Ranvier (i.e., the length of myelin sheaths, commonly referred to as internodes) [2]. Changes in axonal myelination can therefore alter conduction speeds and thus contribute to the regulation of neuronal network communication. Over recent years, it has become clear that myelination is dynamic and responsive to experience [3–5]. Social isolation impairs myelination in the prefrontal cortex of juvenile and adult mice [6, 7]. Conversely, learning of motor tasks induces white matter changes in humans [8, 9], optogenetic axonal stimulation increases myelination and improves motor function in mice [10], and the genetic blockade of adult myelination impairs learning of complex motor tasks [11]. Therefore, it is plausible that changes in myelination properties, such as myelin sheath length, could be employed to dynamically fine-tune axon conduction within networks. In fact, there is anatomical evidence for sheath length differences to control conduction [12], which opposes the long-standing view that myelin sheath length is in a fixed linear relation to axon diameter [13, 14]. For example, sheath length is highly adapted to precisely control co-incidence of action potential arrival times in the auditory system of gerbils [15]. Furthermore, cortical neurons show completely unpredictable patterns of sparse and discontinuous myelination with currently unclear function [16, 17]. It has been suggested that such atypical anatomical patterns represent adaptations in axonal myelination to modulate nervous system function. This means that the myelination status of axons might be dynamically regulated over time. However, direct evidence for remodeling of existing myelin sheaths is still lacking as adaptive myelin changes were so far observed in correlational studies and may equally reflect *de novo* myelination of previously unmyelinated axons. Similarly, it is not clear whether atypical anatomical myelin patterns reflect plastic adaptations of existing myelin or rather a snapshot of ongoing myelination, which can occur over long periods of time in some CNS regions and during learning [18, 19].

To date, essentially no information exists about the regulation of myelin sheath length over extended periods of time. Such knowledge is not only important for understanding plasticity in axonal myelination, it is equally important to guarantee maintenance of conduction speed during development. Some axons are myelinated very early in life—a time during which the organism still grows substantially while nervous system function needs to be maintained. Some studies have addressed control of myelin sheath length by axons and oligodendrocytes [20–25]. However, no study has yet investigated how axon myelination

patterns with internodes of different length are manifested, and how they might change over time.

To investigate control of sheath length dynamics, it is crucial to follow myelinated axons in the same animal. Although substantial progress has been made in recent years on intravital imaging of oligodendrocyte precursor cells and of myelin in the living rodent CNS [26–29], the intractability of myelin due to its small size and concealment within tightly packed axon tracts makes sufficiently resolved investigations of the dynamics of axonal myelination patterns an inherently difficult endeavor. To overcome these challenges, we have taken advantage of the zebrafish as vertebrate model to carry out long-term high-resolution live cell imaging *in vivo*. Here, we show for the first time how myelin sheaths of different lengths are formed, maintained, and remodeled using longitudinal analysis of individual myelinated axons with their myelin and axonal subdomains during developmental myelination, and after targeted oligodendrocyte ablation.

RESULTS

Variability of Myelin Sheath Length along and across Axons

We aimed to investigate how axon myelination patterns with internodes of different length are established and maintained over time. To do this, we used existing and generated new transgenic reagents and lines to simultaneously label myelin sheaths, myelinated axons, and nodes of Ranvier by targeted expression of fluorescent proteins in the zebrafish spinal cord [30, 31]. We first confirmed that myelin sheaths generated by the same oligodendrocyte can be of variable length, as reported previously in several organisms [30, 32, 33]. Assessment of randomly chosen sheaths in mbp:EGFP-CAAX transgenic animals showed that at 7 days post-fertilization (dpf), sheath length ranged between 4 and 71 μm (32.4 ± 15.6 μm, n = 110/17 sheaths/animals, Figures S1A and S1B) and that individual oligodendrocytes could indeed generate sheaths of the entire spectrum of lengths observed (Figures S1A and S1B). This high degree in variability for individual oligodendrocytes raised the question whether internode length just follows a random stochastic distribution, or whether it is driven by axonal requirements.

Therefore, we analyzed the correlation of sheath length variability with their distribution along and between individual axons. To be able to do this, we generated a new transgenic reagent to visualize nodes of Ranvier along myelinated axons, based on the simple premise that the distance between two nodes reflects the length of the myelin sheath. Co-expression of the new cntn1b:Nfasca-EYFP reporter (a fusion of EYFP to the C terminus of zebrafish Neurofascin (Nfasca), a well-described cell adhesion molecule that localizes to nodes of Ranvier [34]) and of cntn1b:mCherry to label axons resulted in discretely spaced puncta of EYFP fluorescence alongside mCherry-labeled axons (Figure 1A). Triple-labeling with cytoplasmic mCherry and Nfasca-EYFP in axons in transgenic animals that have all myelin labeled by mbp:memCerulean revealed that Nfasca-EYFP puncta localized specifically to the gaps between the memCerulean-labeled myelin sheaths (Figure 1B). In contrast to myelinated axons, Nfasca-EYFP expression appeared diffuse along the axon where no myelin was present (Figure S1C). Given this pattern, we conclude that Nfasca-EYFP can be used to assess spacing of nodes of Ranvier along myelinated axons, and that the distance between two distinct nodes corresponds to the length of the respective myelin sheath. When we assessed sheath length (here inferred from internodal spacing) along fully myelinated axons at 7–8 dpf, it was also variable and ranged between 6 and 87 μm (37.7.9 ± 16.8 μm, n = 143/15/15 sheaths/axons/animals, Figure 1C). However, we noticed that sheaths were overall shorter along some axons and longer along others. Indeed, when we compared length distribution between individual axons, about 50% of the axons analyzed showed significant differences to other axons in a one by one comparison (7/15 axons with $p < 0.05$ in a multiple comparison analysis, n = 15/15 axons/animals). We did not observe major regional differences in the length of myelin sheaths that were located in dorsal and ventral tracts of the spinal cord (Figures 1C and S1B). It is well established that there is an overall correlation between myelin sheath length and axon diameter [13, 14]. However, when we assessed axon size in our light microscopic images (measured axonal area divided by its length), all axons analyzed in our study were around 1 μm in diameter and did not show a significant correlation to sheath length along the respective axon (0.9 ± 0.1 μm, $r = -0.02$; $p = 0.95$; Figure S1D). Therefore, myelin sheath length is more similar along than between individual axons, and can be independent of axon size.

It was recently described that certain cortical neurons in the mouse show discontinuous myelin patterning along their axons [16, 17]. We wondered whether sparse axonal myelination also exists in zebrafish. And if it does, what would the distribution of myelin sheath lengths be along these axons, given that each sheath would have more axonal space to extend into? First, we observed axons that were only partially myelinated (Figures 1D and 1E), reminiscent of previously described patchy myelination along mouse cortical neurons. When we followed individual partially myelinated axons over time, we found that some of them got increasingly myelinated over days of ongoing development (3/6 axons, 6 animals, Figures 1D–F′). However, other partially myelinated axon profiles remained largely stable over the entire period of analysis (3/6 axons, 6 animals, Figures 1E and 1F′). To rule out that the observed partial myelination resulted from incomplete labeling of myelin in our mbp reporter lines, we carried out spectral confocal reflectance microscopy (SCoRe) as a label-free method to identify myelinated axons [27]. Using SCoRe imaging of partially myelinated cntnb:mCherry axons in mbp:EGFP-CAAX lines, we found that the presence and absence of myelin observed in the transgenic reporter highly correlated with the respective presence and absence of axonal reflectance, indicating faithfulness of the transgenic myelin reporter (Figure S1E). Interestingly, these myelin sheaths that had no direct neighbors were not longer than those with neighbors and within the same size range as sheaths along fully myelinated axons (9–68 μm, 23.9 ± 14.9 μm, n = 11/11 axons/animals, Figure 1G).

Differences in Myelin Sheath Length Are Established within the First Days after Their Initiation

The finding that some axons have shorter myelin sheaths while others have longer ones, and that sheaths on sparsely myelinated axons are not longer than the longest seen on fully myelinated axons, raised the question as to how myelination patterns

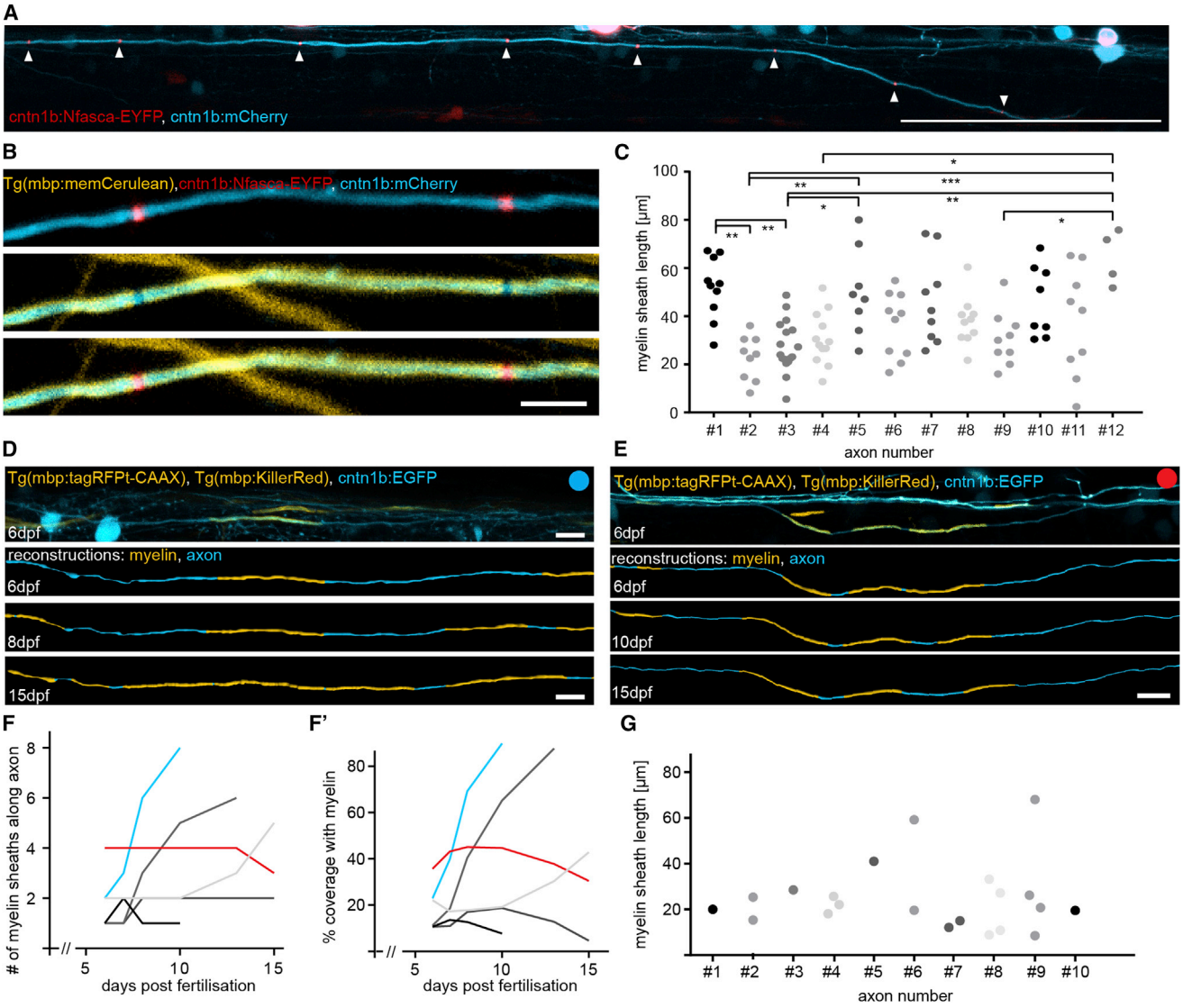

Figure 1. Variability of Myelin Sheath Length along and across Axons

(A) Confocal image of a spinal cord neuron expressing cntn1b:mCherry and cntn1b:Nfasca-EYFP at 7 days post-fertilization (dpf). Scale bar, 100 µm.

(B) Confocal image of a spinal cord neuron expressing cntn1b:mCherry and cntn1b:Nfasca-EYFP in Tg(mbp:memCerulean) transgenic animals at 7 dpf. Scale bar, 10 µm.

(C) Quantification of myelin sheath length (determined by internodal distance) along 12 axons at 7–8 dpf. Axons #1–10 were located in the middle/dorsal tracts of the spinal cord, #11, 12 in the ventral tract (Tukey's multiple comparison test, ANOVA summary: $p < 0.001$, $F(14,128) = 3,986$).

(D and E) Confocal image (top) and timeline of reconstructions of confocal stacks (bottom three) of a partially myelinated cntn1b:EGFP-expressing axon in Tg(mbp:tagRFPt-CAAX), Tg(mbp:KR) transgenic animals showing increasing (D) and stable myelination (E) from 6 to 15 dpf. Scale bar, 10 µm.

(F and F′) Quantification of myelin sheath number along individual axon stretches (F) and the percentage of myelin coverage of this stretch (F′). Examples shown in (D) and (E) are colored blue and red, respectively.

(G) Quantification of myelin sheath lengths along 10 partially myelinated axons at 7–8 dpf.

See also Figure S1.

with sheaths of different lengths become manifested over time. To address this, we have carried out longitudinal studies of individual myelin sheaths from their initiation onward for up to four weeks of animal age (Figures 2 and S2; Movies S1 and S2). Labeling of newly myelinating oligodendrocytes with their nascent myelin sheaths using an olig1:memEYFP reporter construct (Figure S2A) in mbp:memCerulean full transgenic animals was used to assess length changes of individual sheaths from their initiation onward and to determine when it reaches a neighboring sheath (Figures 2A and 2B). We found that, over up to 14 days of analysis, myelin sheaths reached the vast majority of their final length by 3 days post-initiation (dpi) (79% ± 14% in a 7-day analysis, n = 24/6 sheaths/animals; 72% ± 6% in a 13- to 14-day analysis, n = 11/3 sheaths/animals). During the first 3 days after sheath initiation, we saw highly variable rates of length changes ranging between −6 and

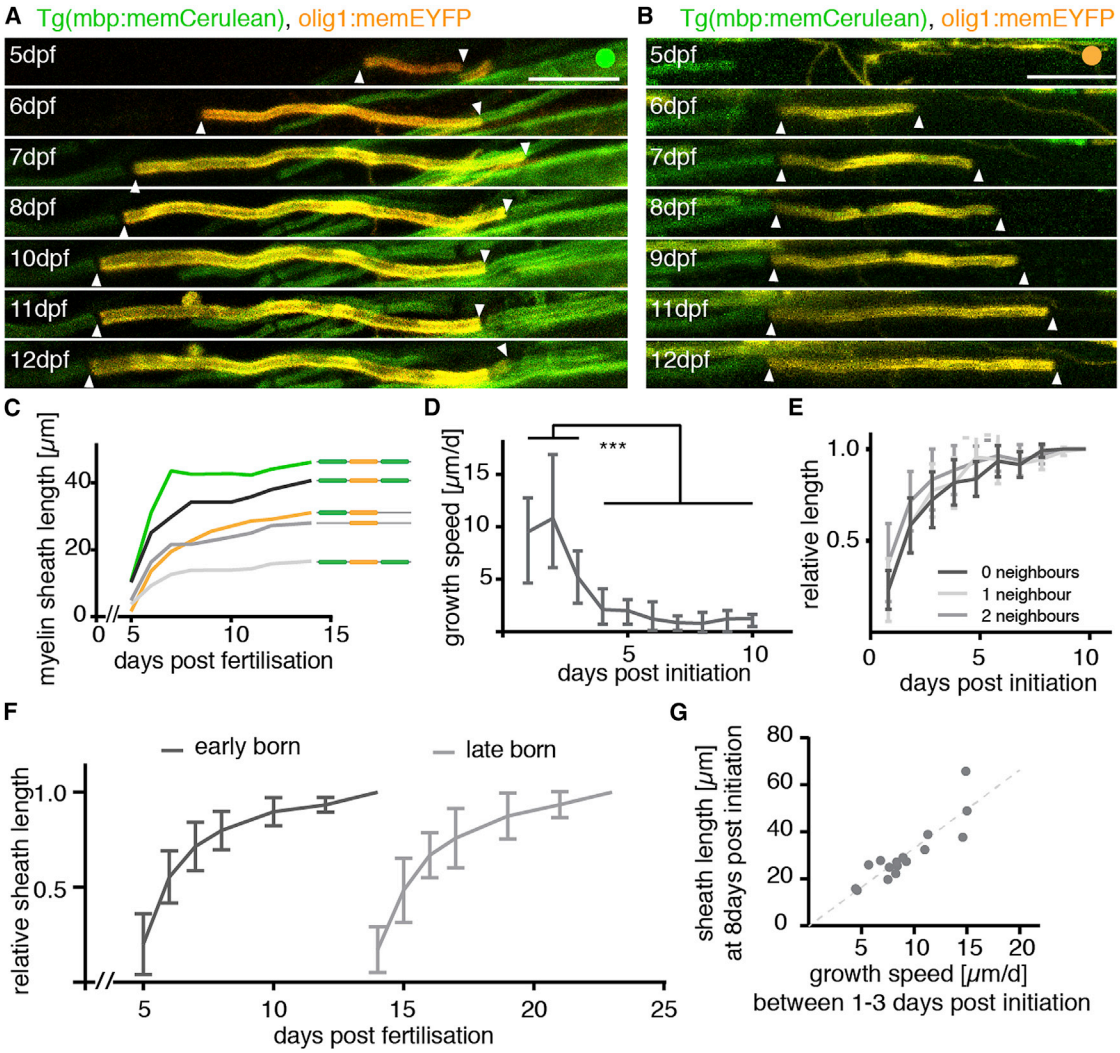

Figure 2. Differences in Myelin Sheath Lengths Are Established within a Few Days after Their Initiation

(A) Timeline of confocal images of an olig1:memEYFP-labeled myelin sheath in a Tg(mbp:memCerulean) background between 5 and 12 days post-fertilization (dpf) getting flanked by two neighboring sheaths over the course of analysis (arrowheads). Scale bar, 10 μm.

(B) Timeline of confocal images as in A showing an individual sheath flanked by only one neighbor (arrowheads). Scale bar, 10 μm.

(C) Quantification of the length of five example sheaths between 5 and 14 dpf.

(D) Quantification of growth speeds of individual sheaths between 1 and 10 days post-initiation (dpi). Data are expressed as median with interquartile range (Wilcoxon matched-pairs signed-rank test, $p < 0.001$).

(E) Quantification of the relative length increase of sheaths with two, one, or no neighboring sheath by the end of analysis. Data are expressed as mean ± SD.

(F) Quantification of the relative length increase of sheaths initiated at 5 and 14 dpf, respectively. Data are expressed as mean ± SD.

(G) Correlation of sheath growth speed from 1 to 3 dpi with its length at 8 dpi.

See also Figure S2 and Movies S1 and S2.

41 μm/day, meaning that individual myelin sheaths either shrunk, grew, or remained stable (9.3 ± 4.2 μm/day, n = 77/13 sheaths/animals, Figures 2C and 2D). After this time (from 4 to 10 dpi), myelin sheaths continued to change length, albeit at much slower rates ranging between −7 and +11 μm/day (1.6 ± 1.7 μm/day, $p < 0.001$, n = 74/12 sheaths/animals), so that length differences between sheaths did not change much further (Figures 2C and 2D). This pattern of variable fast growth during the first 3 days, followed by slow and similar growth over the following days was independent of whether a myelin sheath had two, one, or no neighboring sheaths at the end of the analysis. In all cases, about 3/4 of their end length were established by day 3 of an 8 ± 1 days analysis (83% ± 17% versus 78% ± 15% versus 72% ± 15%, n = 12, 13, 14/39 sheaths, $p = 0.2$, Figure 2E). Furthermore, myelin sheaths that were initiated at much later larval (14 dpf) stages of animal development also showed the same growth pattern as sheaths in younger animals (5 dpf). In both cases, about 70% of sheath length were established by day 3 of a 10- to 11-day analysis (72% ± 13% versus 69% ± 12%, from 5 dpf versus 14 dpf, n = 13/3 versus 8/2 sheaths/animals, $p = 0.71$, Figure 2F). In fact, for all myelin sheaths analyzed, regardless of their time of initiation and

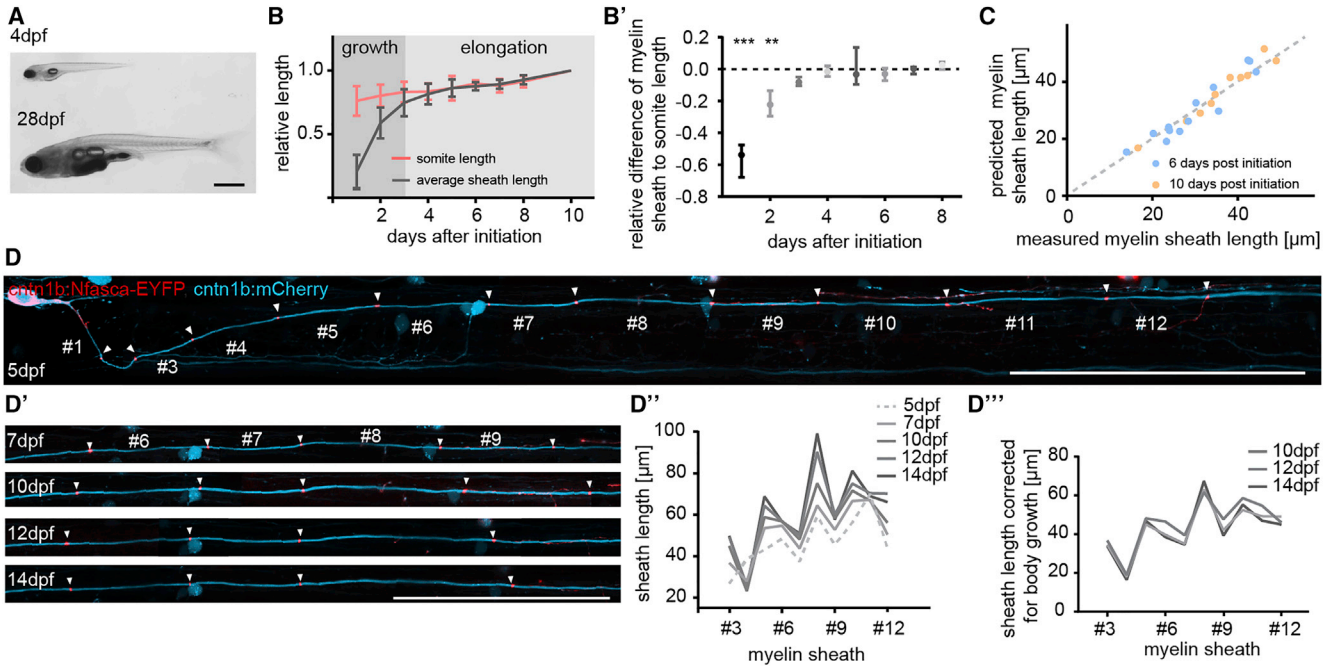

Figure 3. Long-Term Extension of Myelin Sheaths Compensates for Body Growth

(A) Photographs of zebrafish at 4 and at 28 days post-fertilization (dpf). Scale bar, 1 mm.

(B) Quantification of the relative increase of sheath length from their respective initiation onward compared to the increase in somite length over the same time. Data are expressed as mean ± SD.

(B′) Quantification shown in (B) corrected for increase in body growth. Data are expressed as median with interquartile range (Wilcoxon signed-rank test).

(C) Correlation between measured sheath length and their predicted length using increase in somite size as a reference.

(D–D‴) Timeline of confocal images of an individual cntn1b:mCherry, cntn1b:NFacsa-EYFP co-expressing neuron in the zebrafish spinal cord between 5 and 14 dpf. Scale bar, 100 µm (D and D′).

(D″) Quantification of sheath lengths along the axon shown in (D) between 5 and 14 dpf.

(D‴) Quantification shown in (D″) corrected for animal body growth.

See also Figure S2 and Movie S2.

presence/absence of neighboring sheaths, the growth speed during the first days was sufficient to determine whether the myelin sheath was relatively short or long at end of analysis. Plotting the daily growth rates from 1 to 3 dpi against the respective length at 8 dpi revealed a high correlation between early growth and eventual length ($r = 0.87$, $n = 16$ internodes, $p < 0.001$, Figure 2G). We therefore conclude that differences in individual myelin sheath length are established during the first days after their initiation.

Mature Myelin Sheaths Continue to Elongate at Similar Rates to Compensate for Body Growth

Although the majority of sheath growth occurred during the first days of their respective initiation, we observed that they never fully stopped extending during the entire time of analysis (Figures 2C–2F). Most animals, including humans, grow while they have myelinated axons, and their function needs to be maintained during this time. We therefore wondered whether the slow but continuous extension of established myelin sheaths is to compensate for body growth during zebrafish development, which hugely increases in overall size over the time of analysis (Figure 3A). To determine whether a correlation between sheath extension and body growth exists, we assessed the increase of the animals' somite length (a reliable proxy for animal growth) in addition to the extension of established myelin sheaths in the same animal from 3 days after their respective initiation onward. Indeed, we found that the relative length increase of myelin sheaths extended at the same rate as somite length did in the respective animal (Figures 3B and S2B). Comparison of the difference in relative sheath and somite length at different time points after sheath initiation only revealed a significant difference during the first 2 days of its growth, but not after this time (Figures 3B′ and S2D for exact numbers and p values). Interestingly, it was possible to use the increase in somite length as a factor to reliably predict extension rates of myelin sheaths that are older than 3 days (correlation coefficient of 0.95 at 6 dpi, and 0.98 at 10 dpi, $p < 0.001$, $n = 13$ and 10, Figure 3C).

The rapid determination of myelin sheath length differences also led to the question whether axon myelination patterns change over time. To investigate myelin sheath length distribution changes along axons, we analyzed node of Ranvier position by cntn1b:Nfasca-EYFP labeling along individual cntn1b:mCherry-labeled axons starting at 4 dpf, i.e., from shortly after the onset of spinal cord myelination in zebrafish at 3 dpf. As noted in the analysis of sheath length along partially myelinated axons (Figure 1F), individual axons got increasingly myelinated at different rates. During the time of increasing myelin coverage, axon myelination patterns also showed big changes, as new

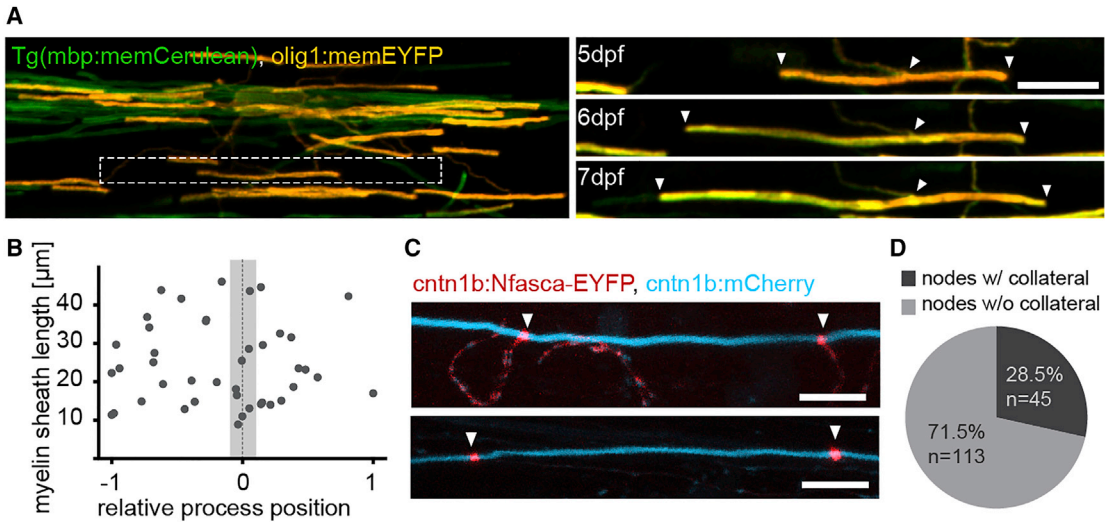

Figure 4. Evidence for Control of Myelin Sheath Length and Positioning by Axons

(A) Timeline of confocal images of an olig1:memEYFP-labeled oligodendrocyte in a transgenic Tg(mbp:memCerulean) zebrafish between 5 and 7 days post-fertilization (dpf). Scale bar, 10 μm. Arrowheads depict the feeding process and the ends of the respective sheath.

(B) Quantification of the position of the oligodendrocyte process relative to its sheath length. −1 and +1 refer to the anterior and posterior end of the sheath, respectively.

(C) Confocal images of cntn1b:mCherry, cntn1b:NFasca-EYFP-expressing myelinated axons with (top) and without (bottom) collateral branches at the node of Ranvier. Scale bar, 10 μm.

(D) Quantification of NFasca-EYFP-labeled nodes of Ranvier with and without collateral axon branches.

See also Movie S1.

sheaths appeared between time points, thus changing the patterning (data not shown). However, once an axon was fully myelinated, relatively short sheaths usually remained short, whereas long ones remained long. When we plotted the length of consecutive myelin sheaths (here inferred by the distance between two NFasca-EYFP puncta) starting from the soma to more distal regions along the same axon over time, each myelinated axon had formed a unique pattern of differential node of Ranvier spacing (Figures 3D and S2C–C‴, n = 7/7 axons/animals). This analysis of node position along fully myelinated axons over time showed that sheaths could still grow, shrink, and remain stable, as we have observed for individual sheaths (Figure 2). We also detected sheath retractions in some cases (5/60 sheaths), confirming previous studies [31, 35]. However, apart from occasional sheath retractions, each axon maintained its characteristic patterning over time, particularly when sheath length changes were corrected for body growth (Figures 3D″, 3D‴, and S2C–S2C‴). In summary, our data show that differences in myelin sheath length were established by dynamic growth within the first 3 days after their initiation. After this time, sheaths continue to extend at similar rates to compensate for body growth. In consequence, axon myelination patterns remained largely stable over time.

Myelin Sheath Growth Can Be Restricted by Axon Collateral Branches

The described stereotypical pattern of myelin sheath growth raises the question how it might be controlled by axons. Our finding that sheaths along partially myelinated axons are not abnormally long (Figure 1G) indicates that axonal landmarks might exist to prevent the sheaths from growing further. In support of this idea, we regularly noted that sheaths grew asymmetrically along axons (Figure 4A). By labeling of individual myelin sheaths with olig1:memEYFP in Tg(mbp:memCerulean) animals over time, we frequently observed increased extension into one direction over the other, despite the absence of neighboring sheaths as a potential physical barrier (Figure 4A). Indeed, determination of the position where the oligodendrocyte process feeds into the sheath in randomly chosen sheaths in full transgenic mbp reporter lines revealed that the vast majority of myelin sheaths had grown asymmetrically. About 80% of all sheaths analyzed had the cell process feeding into the respective sheath outside a 10% region around their center (34/42 sheaths in 16 animals, Figure 4B). One possible explanation for such asymmetric growth of isolated sheaths could be axonal physical barriers. Indeed, we observed that some axons displayed collateral branches when we labeled them with a cntn1b fluorescent protein reporter. When we followed such collaterals over time, we found that the presence of an axon collateral before myelination always coincided with the future position of the node of Ranvier (12/12 nodes, n = 6/6 axons/animals, Figure 4C). However, only a third of all NFasca-EYFP nodes analyzed also showed collateral axon branches (28.5%, 45/158 nodes on 15 axons, Figure 4D). In conclusion, the polarized myelin sheath growth that we frequently saw can be explained by the presence of axon collateral branches in some, but not all cases.

Dynamic Remodeling of Myelin Sheath Length in Response to Targeted Oligodendrocyte Ablation

Because cessation of myelin sheath growth frequently occurred in the absence of obvious barriers, we wondered whether the axon has permissive and non-permissive areas for myelin

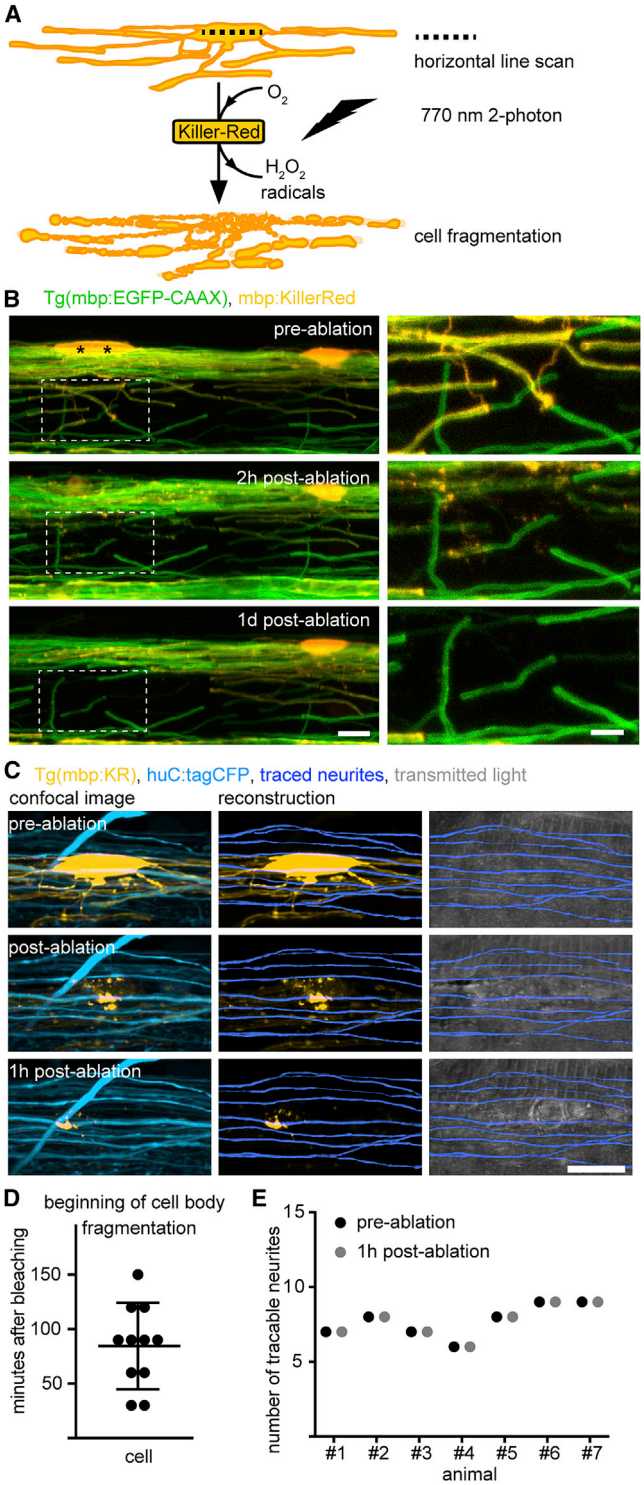

Figure 5. Targeted Ablation of Individual Oligodendrocytes without Causing Bystander Axon Damage

(A) Schematic drawing of single oligodendrocyte ablation using two-photon bleaching of mbp:KillerRed-labeled cells.

(B) Timeline of confocal images of individual mbp:KillerRed-expressing oligodendrocytes in Tg(mbp:EGFP-CAAX) full transgenic zebrafish at 7 days post-fertilization (dpf) before and after two-photon bleaching of the cells marked by the asterisk. Scale bars, 10 μm (left), 5 μm (right).

(C) Confocal images and axon reconstructions of huC:tagCFP-labeled axons in Tg(mbp:KillerRed) zebrafish before and after oligodendrocyte ablation at 4 dpf. Scale bar, 10 μm.

(D) Quantification of the beginning of cell body disintegration after two-photon bleaching of mbp:KillerRed-expressing cells at 4 dpf. Data are expressed and mean ± SD.

(E) Quantification of traced neurites in direct proximity to the ablation site before and after oligodendrocyte ablation as shown in (C).

See also Figure S3 and Movie S3.

sheaths to extend into. To test this, we have developed an assay for rapid and precise oligodendrocyte ablation that enables us to remove individual sheaths along myelinated axons. In this paradigm, parts of axonal surface permissive for myelination would be revealed and could be occupied by neighboring established sheaths, provided they are able to dynamically remodel. To ablate oligodendrocytes, we labeled them by expression of the photosensitizer KillerRed, which generates reactive oxygen species upon green light illumination [36], and which has been used to ablate zebrafish neurons [37]. While bleaching of mbp:KillerRed with green light was of limited success to ablate oligodendrocytes (data not shown), bleaching with 770-nm two-photon laser light resulted in highly efficient disintegration of the oligodendrocyte soma within 1–2 hours (84 ± 38 minutes, n = 11/6 cells/animals), and the fragmentation of myelin sheaths soon after that (Figures 5A, 5B, 5D, and S3A; Movie S3). Importantly, this method did not lead to obvious damage of surrounding axons, as shown by tracing huC:tagCFP-labeled axons in immediate proximity to the myelinating cell body before and after cell ablation (n = 54/7 axons/animals, Figures 5C, 5E, and S3B).

In order to test whether established myelin sheaths are able to remodel, we identified single KillerRed-labeled sheaths that were flanked by KillerRed negative sheaths on either side. We then ablated the corresponding oligodendrocyte at a time point after which myelin sheaths had reached their predictable extension phase. In all ablations (17/17), we observed myelin remodeling, which involved dynamic length changes of neighboring sheaths and/or the formation of new myelin sheaths (Figure 6; Movies S4, S5, and S6). Remodeling was typically characterized by the following sequence of events: (1) the extension of the neighboring sheaths into the demyelinated gap from 1 day post-ablation (dpa) (76% of all cases [13/17]; sheaths did not extend in the remaining cases), (2) the formation of a new myelin sheath in the remaining gap between 2 and 4 dpa (80% of all observable cases (12/15); in three cases, the neighboring sheaths closed the gap and formed a nodal gap), (3) a pushing back of the neighboring myelin by the newly formed sheath (80% of observable cases [8/10]; in 6 cases, the new sheath pushed back neighbors that had invaded the demyelinated territory; in two cases, the new sheath pushed neighbors that had not grown into the gap) (Figures 6A and 6D). The growth rates of remodeling and newly formed myelin sheaths also greatly differed from the highly predictable rates seen normally for myelin of that age (Figures 6B and 6C). Comparison of sheath length changes in the ablation paradigm with their predicted changes revealed that sheaths neighboring the ablation site re-initiated growth at an about 8-fold higher rate than it was predicted by correlation with animal growth (4.5 ± 3.0 versus 0.6 ± 0.5 μm/day at 1–3 dpa, p = 0.04, n = 5/4 sheaths/animals, Figures 6A′ and

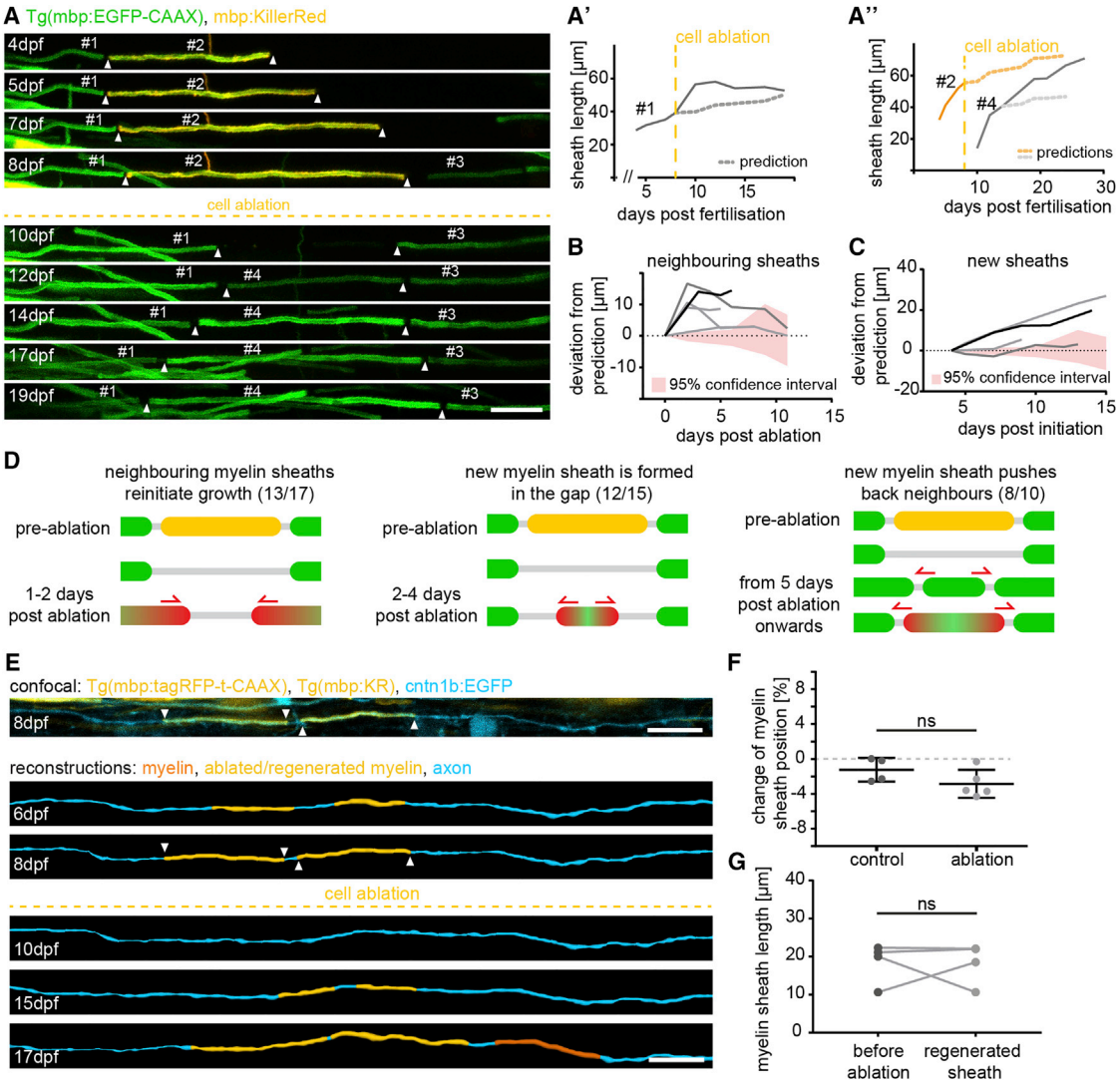

Figure 6. Myelin Sheaths Dynamically Remodel after Targeted Oligodendrocyte Ablation

(A–A′′) Timeline of confocal images of the formation of three consecutive sheaths, ablation, and subsequent remodeling between 4 and 19 days post-fertilization (dpf). (A′) shows the quantification of growth curves of sheath #1 over the time of analysis and its predicted growth (dotted line) based on its age and animal body growth. (A′′) shows the quantifications of the measured sheaths #2 and #4 as seen in (A), and the respective predicted growth (dotted lines) described in (A′). Scale bar, 10 μm.

(B) Quantification of deviated growth of individual sheaths neighboring the ablation site.

(C) Quantification-deviated growth of new sheaths formed in the ablation site.

(D) Schematic summarizing the frequency of observed/possibly observable events of sheath growth and remodeling.

(E) Top: confocal image of discontinuously myelinated axons labeled with cntn1b:EGFP in a Tg(mbp:KR), Tg(mbp:tagRFPt-CAAX) transgenic animal at 8 dpf. Below: reconstructions of the same axon shown above at different time points before and after oligodendrocyte ablation between 6 and 17 dpf. Scale bar, 10 μm.

(F) Quantification of the relative position of regenerated sheaths and the relative position of control sheaths along discontinuously myelinated axons over the same time. Data are expressed as mean ± SD (t test, $t(7) = 1.598$, $p = 0.15$).

(G) Quantification of sheath length before and after ablation along discontinuously myelinated axons (t test, $t(3) = 0.0592$, $p = 0.96$).

See also Movies S4, S5, and S6.

6B). In addition, newly formed myelin sheaths showed nearly 4-fold higher growth rates in the remodeling paradigm compared to primary myelination from 4 dpi onward, a time point at which sheaths usually were in their slow and predictable extension phase (2.3 ± 0.9 versus 0.6 ± 0.1 μm/day growth from 4 to 5 dpi for up to 15 days, $p = 0.04$, $n = 4/3$ sheaths/animals, Figures 6A′′ and 6C). Together, this shows that established myelin sheaths are able to dynamically remodel and to grow at faster rates than they normally would.

Interestingly, when we were able to follow remodeling myelin sheaths for long enough (at least until 8 dpa, 6 cases), we could even observe the re-establishment of sheath lengths that were present prior to ablation in 50% of the cases (Figures 6A and 6D). The re-establishment of the pre-ablation pattern suggested

to us that there may be a memory for myelin sheath positioning, at least along some axons. To further test this idea, we ablated myelinating oligodendrocytes that formed myelin sheaths on only partially myelinated axons. Here, when new sheath(s) were formed, they were very similar with regard to position and length along the otherwise unmyelinated axon as it was before ablation. Indeed, the relative position of the newly formed myelin sheath differed less than 5% to the pre-ablation sheath, which was insignificantly different to control myelin sheaths over the same time (−2.8% ± 1.6% deviation, n = 5/4 sheaths/axons versus −1.2% ± 1.4% n = 4/2 sheaths/axons in control, p = 0.15 Figures 6E and 6F). Myelin sheath lengths before ablation and after regeneration showed also no major differences (18.5 ± 5.3 μm versus 18.3 ± 5.4 μm p = 0.96, n = 4/3 sheaths/animals, Figure 6G). In conclusion, our data provide evidence for a tight axonal control of myelination patterns, because a re-establishment of the pre-ablation pattern along both fully and partially myelinated axons was frequently achieved by the targeted positioning of new myelin sheaths and by the dynamic remodeling of established sheaths.

DISCUSSION

The length of myelin sheaths is an important parameter to regulate speed of axon conduction. Here, we have shown for the first time how axon myelination patterns and myelin sheath length are manifested and provide direct evidence for dynamic sheath remodeling. Our analyses revealed that length differences between individual myelin sheaths are largely established during the first 3 days after their respective initiation—a time period of highly variable and polarized growth along the axon. Afterward, sheaths continue to extend at a low and more similar rate to compensate for animal body growth. As a consequence, spacing patterns of nodes of Ranvier along a given axon are usually maintained over long periods of time once they were established. It remains open for how long sheath extension can occur to compensate for developmental axon and body elongation. Myelin sheaths cannot reach an indefinite length without causing failure of action potential initiation at the next node of Ranvier [34]. One possibility would be the formation of a new sheath at a node of Ranvier by splitting the node into two. Although not observed in this study, our demonstration of myelin sheath remodeling suggests that node splitting and subsequent adaptation of sheath length is a conceivable mechanism. In addition to compensatory myelin length regulation, our work raises questions relating to the coordination of myelin growth and remodeling to establish specific axon myelination patterns.

What regulates different growth speeds of myelin sheaths? Previous studies have reported that oligodendrocytes derived from different CNS regions intrinsically generate sheaths of different lengths [23]. Our results argue for a local regulation at the axon-myelin interface because, despite all variability in sheath length, it is most similar along the same axon. Intrinsic and extrinsic control of sheath length are not mutually exclusive mechanisms and can co-exist in form of a default basal and a regulated rate of myelin growth—a recently proposed hypothesis to integrate default and adaptive mechanisms of myelination [38]. Indeed, other studies have revealed that axonal activity stabilizes nascent sheaths [39], and two recent publications have shown that calcium signaling events in young myelin sheaths, which were in parts induced by axonal activity, can regulate their extension, stabilization, and retraction [24, 25]. We have frequently observed asymmetric growth of young myelin sheath in our study. It would be interesting to know whether this directionality is also in response to axonal activity such as local sites of vesicle release or other features of axonal physiology and architecture.

Independent of the regulatory nature of the growth of young myelin sheaths, they all ceased a few days after their respective initiation, even in the absence of neighboring sheaths and collateral axon branches, which can serve as restricting physical barriers. One possibility is that axons show a differential distribution of instructive (or permissive) and inhibitory axonal factors along myelinated and unmyelinated regions of the same axon, which could regulate sheath extension. The exact molecular nature of regulatory axonal factors remains to be determined, but possible candidates include surface molecules such as PSA-NCAM [40] and Galectin-4 [41], as well as components of the extracellular matrix, which are also of importance for the assembly and maintenance of nodes of Ranvier [42]. These molecules and other node of Ranvier constituents could also serve as landmarks for myelin positioning of regenerating sheaths along partially myelinated axons, which are positioned almost exactly where the ablated ones were. Such landmarks can, however, not explain how length changes for remodeling along fully myelinated axons might be regulated, as the remaining node of Ranvier (the heminode) would have to move together with the myelin sheath along the axon. Our data on sheath remodeling indicate the existence of a homeostatic control of myelin positioning, at least along some axons. We find it complicated to envision how length remodeling, which involves simultaneous growth and shrinkage of neighboring myelin sheaths, can be regulated solely through activity-mediated axon to myelin communication. An alternative possibility would be that axons intrinsically regulate node position—a scenario in which myelin sheaths would extend or shrink rather passively in and out of permissive and non-permissive axonal areas. Future experiments will be required to test the existence of such axon-intrinsic control of node of Ranvier spacing, which could be mediated by retrograde or circuit-based feedback mechanisms in which the axon senses when it functions best. Nodal components are tightly linked to the axon cytoskeleton, along which they may be moved along the axon [43]. An axon intrinsic control of its own myelination pattern would also explain how very precise myelin patterns can emerge along single axons, like the finding that myelin sheaths get progressively shorter toward the Calyx of Held synapse [15].

Myelin sheath length is one of several parameters that affect conduction. We do currently not know how the observed length changes eventually affect axon function. However, in contrast to altering myelin thickness or ion channel density, changing sheath length, which can go along with changes in nodal length, provides a relatively quick regulatory mechanism of axon function, as it was recently proposed [44]. All axons analyzed in this study are parts of spinal locomotor circuits, which need to be functional for coordinated swimming behavior from larval stages onward. It is hence not surprising that myelinated axon patterns establish relatively quickly as we report here. However, we were surprised to see how dynamic myelin sheaths remodel, which

may therefore represent one regulatory mechanism to maintain a functional homeostasis, for example, during naturally occurring death and turnover of single oligodendrocytes [45].

STAR★METHODS

Detailed methods are provided in the online version of this paper and include the following:

- KEY RESOURCES TABLE
- CONTACT FOR REAGENT AND RESOURCE SHARING
- EXPERIMENTAL MODEL AND SUBJECT DETAILS
  - Zebrafish lines and husbandry
- METHOD DETAILS
  - Transgenesis constructs
  - DNA injection and generation of transgenic lines
  - Mounting of zebrafish for live cell microscopy
  - Live cell microscopy and image acquisition
  - Cell ablations
- QUANTIFICATION AND STATISTICAL ANALYSIS
  - Data and statistical analysis
  - Image and data presentation

SUPPLEMENTAL INFORMATION

Supplemental Information includes four figures, one table, and six movies and can be found with this article online at https://doi.org/10.1016/j.cub.2018.01.017.

ACKNOWLEDGMENTS

We are grateful to Wenke Barkey for excellent technical assistance with molecular cloning of the constructs generated for this study and for taking care of the zebrafish colony. We also want to acknowledge Thomas Misgeld for overall support and generous access to microscopy equipment. We thank David Lyons, Mikael Simons, Thomas Misgeld, Laura Hoodless, and all members of the Czopka lab for critical input and discussion of the manuscript. This work was funded by the German Research Foundation DFG (ENP Cz226/1-1 and EXC1010 to T.C.) and a Gertrud Reemtsma PhD student fellowship of the Max-Planck-Society to F.A.

AUTHOR CONTRIBUTIONS

Conceptualization, F.A. and T.C.; Methodology, F.A. and T.C.; Investigation, F.A. and S.V.; Formal Analysis, F.A. and S.V.; Visualization, F.A., S.V., and T.C.; Writing – Original Draft, F.A. and T.C.; Funding Acquisition, F.A. and T.C.

DECLARATION OF INTERESTS

The authors declare no competing interests.

Received: December 1, 2017
Revised: January 4, 2018
Accepted: January 8, 2018
Published: February 8, 2018

REFERENCES

1. Simons, M., and Nave, K.-A. (2015). Oligodendrocytes: Myelination and axonal support. Cold Spring Harb. Perspect. Biol. *8*, a020479.
2. Waxman, S.G. (1980). Determinants of conduction velocity in myelinated nerve fibers. Muscle Nerve *3*, 141–150.
3. Mount, C.W., and Monje, M. (2017). Wrapped to adapt: Experience-dependent myelination. Neuron *95*, 743–756.
4. Forbes, T.A., and Gallo, V. (2017). All wrapped up: Environmental effects on myelination. Trends Neurosci. *40*, 572–587.
5. Fields, R.D. (2015). A new mechanism of nervous system plasticity: Activity-dependent myelination. Nat. Rev. Neurosci. *16*, 756–767.
6. Liu, J., Dietz, K., DeLoyht, J.M., Pedre, X., Kelkar, D., Kaur, J., Vialou, V., Lobo, M.K., Dietz, D.M., Nestler, E.J., et al. (2012). Impaired adult myelination in the prefrontal cortex of socially isolated mice. Nat. Neurosci. *15*, 1621–1623.
7. Makinodan, M., Rosen, K.M., Ito, S., and Corfas, G. (2012). A critical period for social experience-dependent oligodendrocyte maturation and myelination. Science *337*, 1357–1360.
8. Scholz, J., Klein, M.C., Behrens, T.E.J., and Johansen-Berg, H. (2009). Training induces changes in white-matter architecture. Nat. Neurosci. *12*, 1370–1371.
9. Bengtsson, S.L., Nagy, Z., Skare, S., Forsman, L., Forssberg, H., and Ullén, F. (2005). Extensive piano practicing has regionally specific effects on white matter development. Nat. Neurosci. *8*, 1148–1150.
10. Gibson, E.M., Purger, D., Mount, C.W., Goldstein, A.K., Lin, G.L., Wood, L.S., Inema, I., Miller, S.E., Bieri, G., Zuchero, J.B., et al. (2014). Neuronal activity promotes oligodendrogenesis and adaptive myelination in the mammalian brain. Science *344*, 1252304.
11. McKenzie, I.A., Ohayon, D., Li, H., de Faria, J.P., Emery, B., Tohyama, K., and Richardson, W.D. (2014). Motor skill learning requires active central myelination. Science *346*, 318–322.
12. Seidl, A.H. (2014). Regulation of conduction time along axons. Neuroscience *276*, 126–134.
13. Ibrahim, M., Butt, A.M., and Berry, M. (1995). Relationship between myelin sheath diameter and internodal length in axons of the anterior medullary velum of the adult rat. J. Neurol. Sci. *133*, 119–127.
14. Murray, J.A., and Blakemore, W.F. (1980). The relationship between internodal length and fibre diameter in the spinal cord of the cat. J. Neurol. Sci. *45*, 29–41.
15. Ford, M.C., Alexandrova, O., Cossell, L., Stange-Marten, A., Sinclair, J., Kopp-Scheinpflug, C., Pecka, M., Attwell, D., and Grothe, B. (2015). Tuning of Ranvier node and internode properties in myelinated axons to adjust action potential timing. Nat. Commun. *6*, 8073.
16. Tomassy, G.S., Berger, D.R., Chen, H.H., Kasthuri, N., Hayworth, K.J., Vercelli, A., Seung, H.S., Lichtman, J.W., and Arlotta, P. (2014). Distinct profiles of myelin distribution along single axons of pyramidal neurons in the neocortex. Science *344*, 319–324.
17. Micheva, K.D., Wolman, D., Mensh, B.D., Pax, E., Buchanan, J., Smith, S.J., and Bock, D.D. (2016). A large fraction of neocortical myelin ensheathes axons of local inhibitory neurons. eLife *5*, e15784.
18. Miller, D.J., Duka, T., Stimpson, C.D., Schapiro, S.J., Baze, W.B., McArthur, M.J., Fobbs, A.J., Sousa, A.M., Sestan, N., Wildman, D.E., et al. (2012). Prolonged myelination in human neocortical evolution. Proc. Natl. Acad. Sci. USA *109*, 16480–16485.
19. Xiao, L., Ohayon, D., McKenzie, I.A., Sinclair-Wilson, A., Wright, J.L., Fudge, A.D., Emery, B., Li, H., and Richardson, W.D. (2016). Rapid production of new oligodendrocytes is required in the earliest stages of motor-skill learning. Nat. Neurosci. *19*, 1210–1217.
20. Hamilton, N.B., Clarke, L.E., Arancibia-Carcamo, I.L., Kougioumtzidou, E., Matthey, M., Káradóttir, R., Whiteley, L., Bergersen, L.H., Richardson, W.D., and Attwell, D. (2017). Endogenous GABA controls oligodendrocyte lineage cell number, myelination, and CNS internode length. Glia *65*, 309–321.
21. Koudelka, S., Voas, M.G., Almeida, R.G., Baraban, M., Soetaert, J., Meyer, M.P., Talbot, W.S., and Lyons, D.A. (2016). Individual neuronal subtypes exhibit diversity in cns myelination mediated by synaptic vesicle release. Curr. Biol. *26*, 1447–1455.
22. Etxeberria, A., Hokanson, K.C., Dao, D.Q., Mayoral, S.R., Mei, F., Redmond, S.A., Ullian, E.M., and Chan, J.R. (2016). Dynamic modulation of myelination in response to visual stimuli alters optic nerve conduction velocity. J. Neurosci. *36*, 6937–6948.

23. Bechler, M.E., Byrne, L., and ffrench-Constant, C. (2015). CNS myelin sheath lengths are an intrinsic property of oligodendrocytes. Curr. Biol. *25*, 2411–2416.
24. Baraban, M., Koudelka, S., and Lyons, D.A. (2018). Ca 2+ activity signatures of myelin sheath formation and growth in vivo. Nat. Neurosci. *21*, 19–23.
25. Krasnow, A.M., Ford, M.C., Valdivia, L.E., Wilson, S.W., and Attwell, D. (2018). Regulation of developing myelin sheath elongation by oligodendrocyte calcium transients in vivo. Nat. Neurosci. *21*, 24–28.
26. Hughes, E.G., Kang, S.H., Fukaya, M., and Bergles, D.E. (2013). Oligodendrocyte progenitors balance growth with self-repulsion to achieve homeostasis in the adult brain. Nat. Neurosci. *16*, 668–676.
27. Schain, A.J., Hill, R.A., and Grutzendler, J. (2014). Label-free in vivo imaging of myelinated axons in health and disease with spectral confocal reflectance microscopy. Nat. Med. *20*, 443–449.
28. Romanelli, E., Sorbara, C.D., Nikić, I., Dagkalis, A., Misgeld, T., and Kerschensteiner, M. (2013). Cellular, subcellular and functional in vivo labeling of the spinal cord using vital dyes. Nat. Protoc. *8*, 481–490.
29. Hill, R.A., Patel, K.D., Goncalves, C.M., Grutzendler, J., and Nishiyama, A. (2014). Modulation of oligodendrocyte generation during a critical temporal window after NG2 cell division. Nat. Neurosci. *17*, 1518–1527.
30. Almeida, R.G., Czopka, T., ffrench-Constant, C., and Lyons, D.A. (2011). Individual axons regulate the myelinating potential of single oligodendrocytes in vivo. Development *138*, 4443–4450.
31. Czopka, T., ffrench-Constant, C., and Lyons, D.A. (2013). Individual oligodendrocytes have only a few hours in which to generate new myelin sheaths in vivo. Dev. Cell *25*, 599–609.
32. Murtie, J.C., Macklin, W.B., and Corfas, G. (2007). Morphometric analysis of oligodendrocytes in the adult mouse frontal cortex. J. Neurosci. Res. *85*, 2080–2086.
33. Chong, S.Y.C., Rosenberg, S.S., Fancy, S.P.J., Zhao, C., Shen, Y.-A.A., Hahn, A.T., McGee, A.W., Xu, X., Zheng, B., Zhang, L.I., et al. (2012). Neurite outgrowth inhibitor Nogo-A establishes spatial segregation and extent of oligodendrocyte myelination. Proc. Natl. Acad. Sci. USA *109*, 1299–1304.
34. Davis, J.Q., Lambert, S., and Bennett, V. (1996). Molecular composition of the node of Ranvier: Identification of ankyrin-binding cell adhesion molecules neurofascin (mucin+/third FNIII domain-) and NrCAM at nodal axon segments. J. Cell Biol. *135*, 1355–1367.
35. Liu, P., Du, J.-L., and He, C. (2013). Developmental pruning of early-stage myelin segments during CNS myelination in vivo. Cell Res. *23*, 962–964.
36. Bulina, M.E., Chudakov, D.M., Britanova, O.V., Yanushevich, Y.G., Staroverov, D.B., Chepurnykh, T.V., Merzlyak, E.M., Shkrob, M.A., Lukyanov, S., and Lukyanov, K.A. (2006). A genetically encoded photosensitizer. Nat. Biotechnol. *24*, 95–99.
37. Teh, C., Chudakov, D.M., Poon, K.-L., Mamedov, I.Z., Sek, J.-Y., Shidlovsky, K., Lukyanov, S., and Korzh, V. (2010). Optogenetic in vivo cell manipulation in KillerRed-expressing zebrafish transgenics. BMC Dev. Biol. *10*, 110.
38. Bechler, M.E., Swire, M., and ffrench-Constant, C. (2017). Intrinsic and adaptive myelination—A sequential mechanism for smart wiring in the brain. Dev Neurobiol *138*, 4443.
39. Hines, J.H., Ravanelli, A.M., Schwindt, R., Scott, E.K., and Appel, B. (2015). Neuronal activity biases axon selection for myelination in vivo. Nat. Neurosci. *18*, 683–689.
40. Charles, P., Hernandez, M.P., Stankoff, B., Aigrot, M.S., Colin, C., Rougon, G., Zalc, B., and Lubetzki, C. (2000). Negative regulation of central nervous system myelination by polysialylated-neural cell adhesion molecule. Proc. Natl. Acad. Sci. USA *97*, 7585–7590.
41. Díez-Revuelta, N., Higuero, A.M., Velasco, S., Peñas-de-la-Iglesia, M., Gabius, H.-J., and Abad-Rodríguez, J. (2017). Neurons define non-myelinated axon segments by the regulation of galectin-4-containing axon membrane domains. Sci. Rep. *7*, 12246.
42. Susuki, K., Chang, K.-J., Zollinger, D.R., Liu, Y., Ogawa, Y., Eshed-Eisenbach, Y., Dours-Zimmermann, M.T., Oses-Prieto, J.A., Burlingame, A.L., Seidenbecher, C.I., et al. (2013). Three mechanisms assemble central nervous system nodes of Ranvier. Neuron *78*, 469–482.
43. Ghosh, A., Sherman, D.L., and Brophy, P.J. (2017). The axonal cytoskeleton and the assembly of nodes of ranvier. Neuroscientist *1*, 1073858417710897.
44. Arancibia-Cárcamo, I.L., Ford, M.C., Cossell, L., Ishida, K., Tohyama, K., and Attwell, D. (2017). Node of Ranvier length as a potential regulator of myelinated axon conduction speed. eLife *6*, e23329.
45. Young, K.M., Psachoulia, K., Tripathi, R.B., Dunn, S.-J., Cossell, L., Attwell, D., Tohyama, K., and Richardson, W.D. (2013). Oligodendrocyte dynamics in the healthy adult CNS: Evidence for myelin remodeling. Neuron *77*, 873–885.
46. Mensch, S., Baraban, M., Almeida, R., Czopka, T., Ausborn, J., El Manira, A., and Lyons, D.A. (2015). Synaptic vesicle release regulates myelin sheath number of individual oligodendrocytes in vivo. Nat. Neurosci. *18*, 628–630.
47. Kwan, K.M., Fujimoto, E., Grabher, C., Mangum, B.D., Hardy, M.E., Campbell, D.S., Parant, J.M., Yost, H.J., Kanki, J.P., and Chien, C.B. (2007). The Tol2kit: A multisite gateway-based construction kit for Tol2 transposon transgenesis constructs. Dev. Dyn. *236*, 3088–3099.

STAR★METHODS

KEY RESOURCES TABLE

REAGENT or RESOURCE	SOURCE	IDENTIFIER
Experimental Models: Organisms/Strains		
Tg(mbp:EGFP-CAAX)ue2	[30]	ZFIN: ZDB-FISH-150901-26749
Tg(mbp:memCerulean)	this paper	N/A
Tg(mbp:tagRFPt-CAAX)	this paper	N/A
Tg(mbp:KillerRed)	this paper	N/A
Oligonucleotides		
For all primers used, see Table S1	this paper	N/A
Recombinant DNA		
p5E(4.2)_olig1	this paper	N/A
p5E_cntn1b	[31]	N/A
p5E_huC	[46]	N/A
p5E_mbp	[30]	N/A
pME_Nfasca_nostop	this paper	N/A
pME_memCerulean	this paper	N/A
pME_memEYFP	this paper	N/A
pME_tagCFP	this paper	N/A
pME_KillerRed	this paper	N/A
p3E_EYFP-pA	this paper	N/A
pDest_Tol2-pA and other clones of the Tol2kit	[47]	N/A
pTol2_cntn1b:Nfasca-EYFP	this paper	N/A
pTol2_huC:tagCFP	this paper	N/A
pTol2_mbp:memCerulean	this paper	N/A
pTol2_mbp:KillerRed	this paper	N/A
pTol2_mbp:tagRFP-CAAX	this paper	N/A
pTol2_olig1(4.2):memEYFP	this paper	N/A
Software and Algorithms		
Fiji	http://fiji.sc/	RRID:SCR_002285
Imaris	Bitplane	RRID:SCR_007370
Imaris FilamentTracer	Bitplane	RRID:SCR_007366
Huygens Essential	Scientific Volume Imaging	RRID:SCR_014237
Graphpad Prism	Graphpad Software	RRID:SCR_015807

CONTACT FOR REAGENT AND RESOURCE SHARING

Further information and requests for resources and reagents should be directed to and will be fulfilled by the lead contact, Tim Czopka (tim.czopka@tum.de).

EXPERIMENTAL MODEL AND SUBJECT DETAILS

Zebrafish lines and husbandry

We used the following existing zebrafish lines and strains: Tg(mbp:EGFP-CAAX) [30], nacre and AB. The following lines have been newly generated for this study: Tg(mbp:memCerulean), Tg(mbp:tagRFPt-CAAX), Tg(mbp:KillerRed). All animals were kept at 28.5 degrees with a 14/10 hour light/dark cycle according to the local animal welfare regulations. All experiments carried out with zebrafish at protected stages have been approved by the government of Upper Bavaria (animal protocols AZ55.2-1-54-2532-199-2015 and AZ55.2-1-54-2532-200-2015 to T.C.).

METHOD DETAILS

Transgenesis constructs

Sequences of all primers used are listed in Table S1. We generated p5E_olig1(4.2) by PCR amplification of a 5.4kb of gene regulatory sequence directly upstream of the start codon of the zebrafish *olig1* gene (Ensembl: ENSDARG00000040948) from genomic DNA of AB wild-types using the primer combination olig1_F_SalI and olig1_R_SacII (Table S1). The PCR product was then cut with KpnI (endogenous restriction site in *olig1* upstream regulatory region) and SacII restriction enzymes to obtain a 4.2kb product of *olig1* upstream regulatory sequence, which was subsequently cloned into p5E_MCS [47].

To generate pME_NFasca_nostop, we PCR amplified the coding sequence of the zebrafish *neurofascin* gene (Ensembl: ENSDART00000112655.3), which contains a Mucin homology domain (aa933-1035, exon22 ff) specific for the neuronal isoform of mammalian Neurofascin-186, from cDNA of 5dpf AB wild-types with the stop codon removed from the 3′ terminus using primers attB1_NFasca_F and attB2R_NFasca_nostop_R (see also Table S1). The PCR product was then recombination cloned into pDONR221 using BP clonase (Invitrogen).

To generate the middle entry clones pME_memCerulean, pME_memEYFP, pME_tagCFP, and pME_KillerRed, the respective coding sequences were PCR amplified from template plasmids using the primer combinations attB1_memC/YFP_F / attB2R_memC/YFP_R, attB1_tagCFP_F / attB2R_tagCFP_R, and attB1_KillerRed_F / attB1_KillerRed_R (Table S1). PCR products were then cloned into pDONR221 using BP clonase (Invitrogen).

To generate the 3′ entry clone p3E_EYFPpA, EYFP was PCR amplified using the primers BamHI_C/YFP_F and EcoRI_C/YFP_R and cloned into pCS2+ using BamHI/EcoRI restriction sites (Table S1). Then, EYFPpA was PCR amplified from this plasmid using the primers attB2_C/YFP_F and attB3R_pA_R (Table S1), and cloned into pDONR_P2P3R using BP clonase (Invitrogen).

The transgenic expression constructs pTol2_olig1(4.2):memEYFP, pTol2_cntn1b:Nfacsa-EYFP, pTol2_huC:tagCFP, pTol2_mbp:memCerulean, pTol2_mbp:KillerRed, pTol2_mbp:tagRFPt-CAAX were generated in multisite LR recombination reactions with the abovementioned entry clones, p5E_cntn1b [31], p5E_mbp [30], p5E_huC [46] and p3E_pA and pDestTol2_pA of the Tol2Kit [47].

DNA injection and generation of transgenic lines

Fertilized eggs at the one cell stage were pressure microinjected with 1nl of a solution containing 5-20ng/μl plasmid DNA, 25-60ng/μl transposase mRNA [47], and 1% phenol red (Sigma Aldrich). Injected animals were either used for mosaic analysis of single cells, or raised to adulthood. To generate stable transgenic lines, adult injected F0 were outcrossed with wild-type animals and embryos were screened for germline transmission of the injected transgene under a fluorescence stereo dissecting microscope (Nikon SMZ18).

Mounting of zebrafish for live cell microscopy

For live cell imaging, embryonic and larval zebrafish were anaesthetized with 0.2mg/ml MS-222 (PHARMAQ, UK) and mounted laterally in 1% ultrapure low melting point agarose (Invitrogen) on a glass coverslip. The coverslip was then flipped upside-down on a glass slide with a ring of high-vacuum grease filled with a drop of 0.2mg/ml MS-222 to prevent drying out of the agarose and physical damage of the animal. After imaging, animals were either sacrificed, or released from the agarose using microsurgery scalpels and kept individually until further use.

Live cell microscopy and image acquisition

Images of embedded zebrafish were taken at a Leica TCS SP8 confocal laser scanning microscope. Individual myelin sheaths were analyzed from mid trunk regions of the zebrafish spinal cord (between somites 13-24, one example was at somite level 27). Myelin patterns along axons were analyzed throughout the spinal cord (neuron somata resided in somite regions 5-22). We used 448nm and 458nm wavelengths for excitation of Cerulean and tagCFP, 488nm for EGFP, 514nm for EYFP, and 552nm and 561nm for tagRFPt, KillerRed and mCherry. As a standard, we acquired single confocal z stacks as 8 and 12bit images with a pixel size of 114 nm x/y and a z-spacing of 1μm using a 25x, 0.95NA water immersion objective. For high resolution imaging suitable for subsequent deconvolution, we acquired confocal z stacks with a pixel size of 47nm x/y and a z-spacing of 0.25μm using a 40x, 1.1NA water immersion objective. For faster timelapse imaging, we acquired confocal z stacks at 15 and 30 minutes intervals with a z-spacing of 1μm using a 25x, 0.95NA water immersion objective using an 8kHz resonant scanner. For spectral confocal reflectance microscopy (SCoRe), we excited the sample with 488, 561, and 633nm wavelengths and detected reflectance within 5nm around the respective excitation wavelength as described previously [27]. Unless stated otherwise, all images shown are lateral views of the zebrafish spinal cord with anterior to the left and dorsal to the top of the image.

Cell ablations

Mbp:KillerRed expressing cells were ablated using an Olympus FV1000/MPE equipped with a MaiTai DeepSee HP (Newport/Spectra Physics) using a 25x 1.05 NA MP (XLPLN25XWMP) water immersion objective. Continuous confocal scans with a 559nm laser were taken to locate individual labeled oligodendrocytes. The KillerRed expressing cell was then bleached with a 0.5 s line scan across the cell soma using the MaiTai laser tuned to 770nm (1.75W output).

QUANTIFICATION AND STATISTICAL ANALYSIS

Data and statistical analysis

For the analysis of myelin sheath length over time we defined day 1 post initiation (dpi) as the time point when the sheath was first detected during an imaging time line with one day acquisition intervals. Myelin growth speeds are expressed as the length differences between two data points. The growth speed from day 0 to day 1 is defined as the growth speed on day 1. Predicted increases in myelin sheath length were calculated by multiplying the length of an individual sheath at 3dpi with the relative increase in somite length during the same time. To assess axon diameter, we measured the area along a 20μm stretch covered by the axon at three different positions along the axon. The diameter of each axon is expressed as the average value of three areas divided by their respective length. Consecutive myelin sheaths were identified by careful analysis of three-dimensional z stacks over time when they ran in the same focal z-plane and when the opposing sheath ends aligned over time in x and y to form a nodal gap that was not wider than 2 μm (see also Figure S4).

All data were tested for normal distribution using the Kolmogorov-Smirnov normality test. When the sample size was < 5, the Shapiro-Wilk normality test was used. All data are presented as mean ± SD in the running text, independent of normality. In the figures, normally distributed data are shown as mean ± standard deviation (SD), whereas non-normally distributed data are given as median with the 25% and 75% percentiles. All growth curves shown without error bars represent curves of individual myelin sheaths. All grouped curves are shown as mean ± SD and median with the 25% and 75% percentiles, respectively. Data were tested for statistical significance using paired and unpaired t test for normally distributed data, the Wilcoxon matched pairs signed rank test and Mann Whitney test for not normally distributed data. For multiple comparisons ANOVA and Tukey's multiple comparisons test were used. Statistical significance is given as *($p < 0.05$), **($p < 0.01$), and ***($p < 0.001$).

Image and data presentation

Images were analyzed with Fiji and Imaris. Morphology reconstructions were carried out with the Imaris FilamentTracer module. Confocal images were deconvolved with Huygens Essential version 16.10 1p2 (Scientific Volume Imaging, the Netherlands, __http://svi.nl__) when acquired with sufficient oversampling. Data were prepared and assembled using Graphpad Prism 7, Fiji, and Adobe Illustrator CS6.